



UNIVERSITY OF LEEDS

This is a repository copy of *Biom mineralization of a titanium-modified hydroxyapatite semiconductor on conductive wool fibers*.

White Rose Research Online URL for this paper:
<http://eprints.whiterose.ac.uk/119607/>

Version: Accepted Version

Article:

Adamiano, A, Sangiorgi, N, Sprio, S et al. (13 more authors) (2017) Biom mineralization of a titanium-modified hydroxyapatite semiconductor on conductive wool fibers. *Journal of Materials Chemistry B*, 5 (36). pp. 7608-7621. ISSN 2050-750X

<https://doi.org/10.1039/C7TB00211D>

© 2017, The Royal Society of Chemistry. This is an author produced version of a paper published in *Journal of Materials Chemistry B*. Uploaded in accordance with the publisher's self-archiving policy.

Reuse

Items deposited in White Rose Research Online are protected by copyright, with all rights reserved unless indicated otherwise. They may be downloaded and/or printed for private study, or other acts as permitted by national copyright laws. The publisher or other rights holders may allow further reproduction and re-use of the full text version. This is indicated by the licence information on the White Rose Research Online record for the item.

Takedown

If you consider content in White Rose Research Online to be in breach of UK law, please notify us by emailing eprints@whiterose.ac.uk including the URL of the record and the reason for the withdrawal request.



eprints@whiterose.ac.uk
<https://eprints.whiterose.ac.uk/>

Biom mineralization of a titanium-modified hydroxyapatite semiconductor on conductive wool fibers.

Alessio Adamiano ^{a *}, Nicola Sangiorgi ^a, Simone Sprio ^a, Andrea Ruffini ^a, Monica Sandri ^a,
Alessandra Sanson ^a, Pierre Gras ^{b f}, David Grossin ^b, Christine Francès ^f, Konstantinos
Chatzipanagis ^c, Matthew Bilton ^c, Bartosz Marzec ^d, Alessio Varesano ^e, Fiona Meldrum ^d,
Roland Kröger ^c and Anna Tampieri ^a

^a Institute of Science and Technology for Ceramics (ISTEC), National Research Council (CNR),
Via Granarolo 64, 48018 Faenza, Italy

^b CIRIMAT, Université de Toulouse, CNRS/INPT/UPS UMR 5085, Ensiacet, 4 allée Emile
Monso, 31030 Toulouse Cedex 4, France.

^c Department of Physics, University of York, York YO10 5DD, U.K.

^d School of Chemistry, University of Leeds, Woodhouse Lane, Leeds LS2 9JT, U.K.

^e CNR-ISMAL, Institute for Macromolecular Studies, C.so G. Pella 16, 13900 Biella, Italy

^f Laboratoire de Génie Chimique, Université de Toulouse, CNRS/INPT/UPS UMR 5503,
Ensiacet, 4 allée Emile Monso, 31432 Toulouse Cedex 4, France.

Author for correspondence: Dr. Alessio Adamiano

Institute of Science and Technology for Ceramics (ISTEC)
National Research Council (CNR),
Via Granarolo 64, 48018 Faenza (RA), Italy.
E-mail: alessio.adamiano@istec.cnr.it
Tel: +39 0546699761

1 **Abstract**

2 Metal ions are frequently incorporated into crystalline materials to improve their
3 electrochemical properties and to confer new physicochemical properties. Naturally-occurring
4 phosphate apatite, which is formed geologically and in biomineralization processes, has
5 extensive potential applications and is therefore an attractive functional material. In this study,
6 we generate a novel building block for flexible optoelectronics using bio-inspired methods to
7 deposit a layer of photoactive titanium-modified hydroxyapatite (TiHA) nanoparticles (NPs)
8 on conductive polypyrrole(PPy)-coated wool yarns. The titanium concentration in the reaction
9 solution was varied between 8-50 mol% with respect to the phosphorous, which led to titanate
10 ions replacing phosphate in the hydroxyapatite lattice at levels up to 17 mol%. PPy was
11 separately deposited on wool yarns by oxidative polymerization, using two dopants: (i)
12 anthraquinone-2-sulfonic acid to increase the conductivity of the PPy layer and (ii) pyroglutamic
13 acid, to reduce the resistivity of the wool yarns and to promote the heterogeneous nucleation of
14 the TiHA NPs. A specific titanium concentration (25 mol% wrt P) was used to endow the TiHA
15 NPs on the PPy-coated fibers with a desirable band gap value of 3.68 eV, and a specific surface
16 area of 146 m²/g. This is the first time that a thin film of a wide-band gap semiconductor has
17 been deposited on natural fibers to create a fiber-based building block that can be used to
18 manufacture flexible electronic devices.

19

20 **Keywords:** titanium doping; calcium phosphate nanoparticles; wide band gap semiconductor;
21 flexible electronics; biomineralization

1 **1.Introduction**

2 The demand for high performance materials for flexible electronics has motivated the search
3 for building blocks which exhibit specific properties including favourable band gaps, charge
4 carrier mobility, light emission efficiency and quantum yield to construct new electronic
5 devices such as organic and hybrid electronic materials.¹ Doping with metal ions is an effective
6 route for tuning the electronic properties of functional materials, improving their performance
7 and endowing them with new electrochemical properties.^{2,3} Cerium,⁴ tin⁵ and scandium⁶ have
8 been widely used to improve the efficiency of TiO₂-based semiconductors used in dye
9 sensitized solar cells (DSCs), where their incorporation facilitates electron injection by tuning
10 the photoanode band gap and increasing the solar energy conversion efficiency.

11 Metal ions can be also incorporated within phases that do not normally exhibit valuable
12 physico-chemical characteristics to create new materials that are well suited to optoelectronic
13 applications. An excellent example is provided by pure hydroxyapatite (HA, Ca₁₀(PO₄)₆(OH)₂)
14 whose 6.0 eV can be lowered by titanium incorporation to values nearing those of wide band
15 gap semiconductors.⁷ The versatility of this material - that finds numerous industrial
16 applications ranging from water remediation to catalysis⁸⁻¹⁰ is fostered by the readiness with
17 which its lattice can be doped to various extents with monovalent to tetravalent anions and
18 cations,¹¹ to generate HA with tailored properties^{12,13}

19 Doped HA has also attracted considerable attention thanks to its favorable electrochemical
20 properties. Liu et al.¹⁴ reported an increase in the UV absorption of HA nanoparticles (NPs)
21 doped with Fe₃O₄ while other authors showed that Ti-modified HA (TiHA) displays promising
22 photocatalytic activity,^{7,15,16} and good antibacterial properties.¹⁷ Tsukada et al.⁷ reported a band
23 gap energy of 3.65 eV for a Ti⁴⁺ substituted HA with promising performances for the
24 photochemical degradation of small organic molecules like acetaldehyde vapor under UV-VIS

25 radiation, and Wakamura et al.¹⁶ showed that Ti-OH groups on the surface of TiHA can have
26 a positive influence on electron injection, transport rate and short-circuit current density.
27 It is frequently reported that Ti⁴⁺ ions substitute for Ca²⁺ ions in the HA lattice, which results
28 in a modification of its crystal structure¹⁵⁻¹⁸ and phosphate anions can be substituted by titanate
29 anions by annealing of Ti-modified HA at 700-850°C.¹⁹
30 In this work, we report a novel polypyrrole (PPy)/TiHA composite comprising concentric layers
31 of conductive PPy and then the wide band gap semiconductor layer of TiHA NPs on wool yarns,
32 where the TiHA NPs are deposited using a bio-inspired method. The resulting fiber-based
33 structure is a potential building block for use in flexible optoelectronic, such as flexible UV
34 detectors and fabric integrated photovoltaics.
35 HA was chosen as the semiconductor bulk-material because of the simplicity with which it can
36 be nucleated on surfaces by a bio-inspired mineralization approach,²⁰ its functional versatility
37⁸⁻¹⁰ and the well-established photoelectric properties of Ti-modified HAs.^{7,15,16,17,18} Four sets of
38 TiHAs, all of which displayed band gap values comparable those of wide band gap
39 semiconductors²¹⁻²³, were obtained by wet synthesis by adjusting the concentration of the
40 titanium dopant in the growth solution. The TiHA sample displaying optimal properties was
41 then deposited on PPy-coated wool fibers under room temperature by a bio-inspired
42 mineralization, where this ensured that the wool fibers retained their flexibility and softness.
43 These conditions also avoid the growth of coarser TiHA grains that form a brittle coating on
44 the fiber surface that seriously compromise the fiber flexibility and the mechanical stability of
45 the coating. Our successful deposition of thin films of HA on PPy-coated natural fibers
46 therefore delivers a fiber-based building block which can potentially be used to generate a new
47 class of flexible, optoelectronic devices.
48 PPy was chosen as the conductive polymer since it is an established material which has been
49 successfully printed onto Lycra/cotton fabrics to produce resistive fabric strain sensors capable

50 of detecting the posture and gesture of human body.²⁴⁻²⁵ The PPy layer was doped with
51 anthraquinone disulfonic acid (ADA) to improve its electrical conductivity, and with
52 pyroglutamic acid (PyE) to promote the nucleation of the TiHA during mineralization.
53 Oriented self-assembled crystal growth onto various substrates (e.g. Indium Tin Oxide glass,
54 Si/SiO₂ wafers, ZnO thin film etc), including PPy²⁶ for DSC fabrication has been proven
55 succesful.²⁷ However, to the best of our knowledge neither stoichiometric or doped HAs, nor
56 other calcium phosphates were ever mineralized onto a PPy layer, nor on natural fibers, to
57 obtain a fiber-shaped building block for optoelectronic devices.
58 Finally, using a comprehensive combination of Raman and FT-IR spectroscopy, X-ray
59 diffraction, scanning and transmission electron microscopy we performed a detailed
60 characterization of the different components and the fiber-shaped building block.

61

62 **2. Experimental Details**

63 2.1 Synthesis of Titanium-substituted Hydroxyapatite

64 Samples were synthesized by modifying of a previously reported method.¹² Briefly, 10 g of
65 Ca(OH)₂ (purity > 95%, Sigma-Aldrich) were added to 100 mL of Millipore water and then
66 stabilized at 50.0 °C under constant stirring at 400 rpm for 30 min. A solution obtained by
67 mixing 8.87 g of H₃PO₄ (85 wt% Merck) with 30 mL of deionized water was added drop-wise
68 into the Ca(OH)₂ suspension, together with 30 mL of a titanium isopropoxide (purity > 97%
69 Alfa Aesar) solution in isopropyl alcohol (purity ≥ 99.7% Sigma-Aldrich). A titanium-free HA
70 (HAp) was synthesized by simple addition of H₃PO₄ to the Ca(OH)₂ suspension.

71 TiHAs were synthesized using increasing amounts of the titanium precursor to reach the molar
72 percentage of Ti atoms with respect to P of 8%, 17%, 25% and 50%. The obtained TiHAs were
73 named respectively TiHA8, TiHA17, TiHA25, and TiHA50. The molar ratio between Ca and
74 P was set to 1.70 and kept constant for all of the experiments. Once the simultaneous drop-wise

75 addition of phosphoric acid and titanium isopropoxide was performed, the solution was kept at
76 50 °C under constant stirring at 400 rpm for 3 hours and left still at room temperature overnight.
77 Samples were repeatedly washed with water and then freeze-dried. Finally, the obtained
78 powders were ground in a mortar and sieved using a 150 µm mesh filter.

79 2.2 Chemical Analysis

80 The chemical composition of bulk samples was determined by an induced coupled plasma
81 spectrometer (ICP-OES), (Liberty 200, Varian, US) employing wavelengths of 422.673 nm
82 (Ca), 334.941 nm (Ti), and 213.618 nm (P). An aliquot of samples for ICP-OES were dissolved
83 in a diluted HNO₃ solution (~ 2 wt%) prior to analysis.

84 2.3 Powder X-ray Diffraction Analysis (XRD)

85 X-ray diffraction patterns were collected using a D8 Advance Diffractometer (Bruker,
86 Karlsruhe, Germany) equipped with a Lynx-eye position sensitive detector using Cu K α
87 radiation ($\lambda = 1.54178 \text{ \AA}$) generated at 40 kV and 40 mA, operating in the 2θ range between
88 10° and 80° with a step size (2θ) of 0.02° and a counting time of 0.5 s. The same conditions
89 were used to collect diffraction patterns on samples heated at 700°C for 6 hours.
90 Complementary analysis was performed on raw powders using the Diamond Light Source
91 synchrotron beam line I11 (HR-PXRD), where the X-ray diffraction patterns were recorded in
92 the 2θ range between 5° and 70° using a monochromatic radiation (beam energy 15 keV, $\lambda =$
93 0.825969 Å) and a 0.001° step size.

94 The structural and microstructural analysis of the samples was performed using the FullProf
95 suite software,²⁸ based on the Rietveld refinement method and Fourier analysis of the HR-
96 PXRD patterns. A Thompson-Cox-Hastings pseudo-Voigt peak-shape profile was used for the
97 refinement. The microstructural analysis, including both microstrain and crystallite size, was
98 evaluated using the anisotropic Popa approach in the 6/m hexagonal system for the
99 hydroxyapatite structure (R_0 to R_3 refined for anisotropic size factors and E1 to E3 for

100 anisotropic microstrain factors).²⁹ The instrumental contribution to the profile was taken into
101 account by using a LaB₆ instrumental standard. The degree of sample crystallinity was
102 calculated according to Eqn (1):

$$103 \quad \text{Crystallinity}[\%] = 100 \frac{C}{A + C} \quad \text{Eqn(1)}$$

104 where C and A are the sum of peak area and the area between the peaks and the background in
105 the diffraction pattern, respectively.³⁰

106 2.4 Transformed Fourier - Infrared analysis (FTIR) and Raman Spectroscopy.

107 FTIR spectra of the synthesized titanium apatite were collected at room temperature by using
108 an FTIR Nicolet 380 Thermo Electron Corporation spectrometer working in the range of
109 wavenumbers between 4000 cm⁻¹ and 400 cm⁻¹ at a resolution of 2 cm⁻¹. A finely ground,
110 approximately 0.05% (w/w) mixture of the sample in KBr was pressed into a transparent disk
111 using a hydraulic press and applying a pressure in the MPa range. The Infra-red splitting factor
112 (IR-SF) was calculated by adding the measured intensities of the two ν₄(PO₄)₃ vibration bands
113 at 565 and 605 cm⁻¹ in the absorbance mode and dividing their sum by the intensity of the
114 valley between these absorption bands and the baseline, after a baseline correction between
115 1200 and 250 cm⁻¹.³¹

116 TiHA NPs were studied after thermal transformation as described by XRD and Raman
117 spectroscopy. Each sample was placed on a potassium-bromide substrate producing minimal
118 background signal, and the potassium-bromide substrate containing the sample was placed on
119 top of a glass slide in order to fit on the Raman microscope stage for experimentation. The
120 settings used for testing were the following: 532 nm laser, 20-25 mW laser power, 2 seconds
121 acquisition time, 90 accumulations, 50x long working distance lens (spatial resolution ~ 1μm)
122 and 1800T diffraction grating. Decomposition and non-linear curve fitting of the Raman signals
123 were performed on fifteen spectra collected for each sample using Igor Pro 6.37 software.

124 2.5 Zeta potential and Size Measurements

125 ζ -potential distributions of dried powders suspended in HEPES buffer at pH=7.4 were measured
126 by dynamic light scattering (DLS) with a Zetasizer Nano ZS (Malvern Ltd., Worcestershire,
127 UK) and were quantified by laser Doppler velocimetry as electrophoretic mobility using
128 disposable electrophoretic cell (DTS1061, Malvern Ltd., Worcestershire, UK). Ten runs of 30
129 s were performed for each measurement and four measurements were carried out for each
130 sample.

131 Zeta average values were obtained by suspending the dried powders in a 0.1 wt% sodium citrate
132 buffer at pH 6.0. Twenty runs of 30 s each were collected in each measurement and for each
133 sample.

134 2.6 Scanning and Transmission Electron Microscopy

135 The fiber surface morphology was analyzed by a field emission scanning electron microscope
136 (FE-SEM, Carl Zeiss Sigma NTS GmbH Oberkochen, Germany) working at an accelerating
137 voltage in the 1.0 - 5.0 kV range. Fibers were mounted on aluminum stubs using carbon tape
138 and were dried under an IR lamp for 15 minutes before analysis.

139 Sample analysis by transmission electron microscopy was performed at the University of York,
140 JEOL Nanocentre using a JEOL JEM 2011 LaB6 TEM, operating at 200 kV. The microscope
141 was equipped with a Gatan 794 digital camera and a Thermo Fisher NS7 energy dispersive X-
142 ray spectroscopy (EDX) system. Samples were ground using a pestle and mortar, sieved at 150
143 μm , and drop-cast from a methanol suspension onto a holey carbon copper TEM grid.

144 2.7 Thermogravimetric Analysis

145 The carbonate content was evaluated on dried samples by thermogravimetric analysis (TGA)
146 using a Stanton STA 1500 (Stanton, London, UK) apparatus. About 10 mg of apatite was
147 weighed in a platinum crucible and heated from room temperature to 1100 °C under nitrogen

148 flow. The heating rate was 10 °C/min and alumina was used as reference standard. The CO₃²⁻
149 content was evaluated according to the weight loss observed between 550 and 950 °C.³²

150 2.8 Specific Surface Area (SSA)

151 Samples SSA were measured at liquid nitrogen temperature (-196 °C) using Brunauer-Emmet-
152 Teller (BET) mode with a CONTROL 750 (CE Instruments) apparatus. HA powders were dried
153 in air at 100°C for 30 minutes before the analysis.

154 2.9 Determination of Band Gap Values (E_g)

155 For band gap determination and subsequent analysis, a UV-Vis spectrophotometer with an
156 integrating sphere was used. The equipment was calibrated with a Spectralon standard
157 (Labsphere SRS-99-010). The reflectance spectra were measured and converted into an
158 adsorption coefficient using Kubelka-Munk equation while the E_g value was determined from
159 the Tauc plot obtained following the method reported by Sangiorgi et al.³³ Each measurement
160 was carried out three times averaging the recorded values.

161 2.10 Wool and Polypyrrole coatings

162 Wool yarns were obtained from a commercial stock with linear mass density of 68 tex.
163 Polypyrrole (PPy) coated conductive fiber composites were produced by in situ chemical
164 oxidative polymerization of pyrrole (purity > 98% Sigma-Aldrich) on the surface of wool yarns.
165 The polymerization reaction was carried out at room temperature. Different aliquots of
166 antraquinone-2-sulfonic acid sodium salt monohydrate (ADA, purity > 97% Sigma-Aldrich)
167 were added to the pyrrole solutions to enhance PPy conductivity. 0.2 g of pyrrole were dissolved
168 in 20 mL of MilliQ water together with 0.3 g of ADA to obtain a molar ratio ADA/pyrrole of
169 25 mol%. Wool yarns (0.2 g) were soaked in the obtained solution for 5 minutes at room
170 temperature and were then immersed in a Fe(III) solution prepared by dissolving 1 g of
171 FeCl₃·6H₂O (purity > 97% Sigma-Aldrich) in 20 mL of MilliQ water. These two steps were

172 repeated three times. Subsequently, the fibers were rinsed with water, centrifuged, recovered
173 and dried overnight at 40°C. Hereafter, these ADA-doped PPy coated wool fibers are referred
174 to as WAP.

175 PPy doped with pyroglutamic acid (PyE, purity > 99%, Sigma-Aldrich) coated fibers, hereafter
176 referred to as WEAPs, were obtained by adding both ADA and PyE to the pyrrole water solution
177 and following the same steps as described for WAP. Different quantities of PyE, corresponding
178 to the 5.0 mol% (WEAP5) and 10.0 mol% (WEAP10) with respect to the pyrrole, were used to
179 assess the effects of higher amounts of PyE on the conductivity and the nucleation of TiHA 25
180 on WEAPs fibers.

181 2.11 Linear Resistivity

182 Linear resistivity of PPy-coated wool yarns was measured with metal contacts placed 1 cm
183 apart on the yarns using an Escort170 Digital Multimeter. Data were calculated as the average
184 of eight tests. Prior to testing, the PPy-coated yarns were conditioned at 20 °C and 65 % of
185 relative humidity for 24 h.

186 2.12 Bio-inspired mineralization of conductive fibers

187 The procedure described below was followed for the mineralization of WAP and WEAPs fibers.
188 1 g of Ca(OH)₂ and 200 mg of conductive fibers were added to 10 mL of Millipore water. The
189 solution was poured into a closed vessel under magnetic stirring and kept to 50°C for 3 days.
190 After, the solution was poured in a beaker and kept under magnetic stirring while a solution
191 obtained by dissolving 0.87 g of H₃PO₄ in 3 mL of Millipore water was added dropwise
192 simultaneously to a solution of titanium isopropoxide dissolved in isopropyl alcohol to reach a
193 Ti/P molar ratio of 25%, corresponding to the amount of Ti introduced for the synthesis of
194 TiHA25. The solution was then poured again in a closed vessel and placed into a shaking
195 incubator set at 50°C and left under agitation for 7 days.

196 2.13 Deformability and stress tests

197 The flexibility and the mechanical properties of the mineralized wool yarns were evaluated by
198 subjecting mineralized WEAP5 yarns to 10 stretching/release cycles;³⁴ secondly, the
199 deformability of the semiconductor was assessed by knotting WAEP5 yarns before and after
200 mineralization and comparing fibers morphologies by SEM as reported in the literature for other
201 flexible electronic devices.^{35,36}

202 Finally, to assess the endurance to dipping process of the mineral layer, mineralized WAEP5
203 yarns were immersed in ethanol at 40 °C for 15 minutes to simulate a dipping process before
204 being analyzed by SEM to check the eventual removal of the mineral phase from the fibers
205 surface.

206 **3. Results**

207 3.1 TiHA nanoparticles hydrodynamic diameter and ζ -potential

208 The hydrodynamic diameter size distributions of all the samples is reported in Fig. S1, while
209 their average hydrodynamic diameters, expressed as zeta average, with the relative
210 polydispersity indices (Pdi), and the ζ -potentials of TiHA NPs determined by DLS are reported
211 in Table S1. The hydrodynamic diameters of TiHAs increase together with the titanium doping
212 extent, with two step increases: the first moving from TiHA8 to TiHA17, and the second
213 moving from TiHA25 to TiHA50. Differences in the recorded zeta average can be due to a
214 different superficial composition as to the modifications of TiHAs NPs morphology at
215 increasing titanium concentrations. Aggregation seems to play a major role only in the case of
216 TiHA50 NPs, whose hydrodynamic diameter size distribution curve (Fig. S1) shows an
217 enlargement towards larger particles and an higher polydispersity index with respect to those
218 of the other samples (Table S1).

219 Finally, the ζ -potentials of titanium-modified NPs are more negative with respect to that of
220 HAp, with TiHA8, TiHA25, and TiHA50 NPs having similar superficial net charges and
221 TiHA17 NPs having a sensibly more negatively charged surface.

222 3.2 Band gap values of TiHA nanoparticles

223 The band gap energies (E_g) determined using reflectance method and the Tauc equation show
224 values between 3.0 eV and 3.5 eV. These results are suitable for photocatalytic, photovoltaic
225 applications and more in general for optoelectronic applications requiring wide band gap
226 semiconductors. While the experimental bandgap energy of pure HA determined by Tsukada
227 et al. is 6.0 eV, the addition of even small amounts of Ti as in the case of TiHA8 decreases the
228 bandgap to 3.88 ± 0.01 eV, which is a value much closer to that of anatase TiO_2 (3.27 eV).⁷ E_g
229 decreases even further for the other samples containing more Ti and equals 3.73 ± 0.01 eV,
230 3.68 ± 0.02 eV and 3.54 ± 0.01 eV for TiHA17, TiHA25 and TiHA50 respectively. E_g of the
231 mineral phase formed on biomineralized PPy doped fibers is the same as the value recorded for
232 powder samples.

233 3.3 Crystal structure of TiHA nanoparticles after thermal treatment

234 The X-ray diffraction patterns (XRD) shown in Fig. 1 confirm the apatitic structure (JCPDS
235 no. 09-432) of the synthesized powders, including those with high degrees of titanium
236 substitution. The diffraction profiles feature exclusively the typical diffraction peaks of
237 carbonated HA, which tend to become broader with the increase in titanium doping level. A
238 background radiation gain, due to the occurrence of an amorphous phase not detectable by
239 XRD, is observable going from pure HAp to TiHA50. This background noise increases with
240 the increasing doping extent of titanium HAs.

241 The crystallinity index of the powders, together with their cell parameters and the IR-SFs are
242 reported in Table 1. The former decreases as the titanium concentration increases and drop
243 notably compared to TiHA17, while no systematic variation of the lattice parameters with

244 titanium content is detectable by XRD analysis showing little variation and values very close
245 to those of reference HAp for all of the TiHAs. More in detail, the a and c-axes of all the samples
246 are in the range between 9.424 Å – 9.441 Å, and 6.884 Å – 6.894 Å respectively, while the cell
247 volume shows a slight increase from 529.5 for HAp up to 531.7 for TiHA50.

248 The results of the microstructural analysis and the relative HR-PXRD patterns recorded using
249 synchrotron radiation are reported in Table S2 and Fig. S2 respectively. The general crystallite
250 domain is elongated in c-axis direction (approximately 60±4 nm) compared to the perpendicular
251 a/b-axes (24±4 nm.). The strain is also higher in c-axis orientation. Taking into account both
252 the crystallite size and the lattice strain, the apatite domain size is not modified by the
253 introduction of even high amounts of titanium during the synthesis.

254 It is interesting to note that the R-Bragg and the R-structure factors for the Rietveld refinement
255 of TiHA50 slightly improve if titanate (TiO_4^{4-}) substitutes up to 7% of phosphate (PO_4^{3-})
256 (3.73/4.80 compared to 3.76/4.87 for HA structure and 3.91/5.01 for 10% Ti^{4+} substitution of
257 Ca^{2+}).

258 Four peaks potentially corresponding to a second crystalline phase are observed at the 2θ values
259 of 15.63°, 20.82°, 22.74° and 24.93° on TiHA8 and TiHA50 especially. Their resolution is
260 accurately illustrated by the enlarged view of the HR-PXRD spectra collected on the latter
261 sample, reported in Fig. S3. Several structures are tested to identify this phase, among titanium
262 oxide (anatase, rutile and brookite)^{37,38}, calcium phosphate compounds (β-TCP, brushite,
263 monetite, octacalcium phosphate)³⁹⁻⁴², titanium phosphate (TiPO_4)⁴³ and calcium titanium
264 phosphate compounds ($\text{CaTi}_4(\text{PO}_4)_6$).⁴⁴ This last structure matches the experimental pattern but
265 the low number of observed reflections and their low relative intensities do not allow a solid
266 identification.

267 The phase compositions tabulated in Table 2 are obtained by using the Rietveld refinement of
268 the XRD profiles of powders heated at 700°C for 6 hours as reference. Our data show that HAp

269 remained as pure HA phase after the thermal treatment, while for TiHA8 conversion of HA to
270 b-TCP started occurring with no anatase formation. On the contrary, for TiHA with higher
271 doping extents, the formation of a crystalline anatase phase is linearly related to the titanium
272 introduced during the synthesis ($R^2 = 0.9474$ by linear least squares). The formation of b-TCP
273 instead is not linear and reaches its maximum for TiHA17 (23.3 wt%) for which a value much
274 higher with respect to both TiHA8 and TiHA50 is recorded.

275 3.4 Infrared and Raman spectroscopy

276 IR spectra of HAp and TiHAs are shown in Fig. 2. The principal peaks of the spectra recorded
277 on TiHAs are characteristic of apatite and correspond to the absorption band of H₂O (broad
278 peak at 3400 cm⁻¹ and sharper peak at 1640 cm⁻¹), HPO₄²⁻ (1050, 970, 600, and 570 cm⁻¹), and
279 OH⁻ (3570 cm⁻¹). Differences among the spectra are evident when comparing the IR-SFs in
280 Table 1 of the phosphate group absorbing in the spectral region between 650 and 550 cm⁻¹
281 magnified in Fig. 2b. The value of the IR-SF decreases with respect to HAp when titanium is
282 introduced, with the exception of TiHA17 for which a value close to that of HAp is recorded.
283 Another sensible difference is relative to the intensity of the OH librational band (631 cm⁻¹),
284 which is pronounced in the IR spectra of HAp and TiHA25, while it almost disappears for the
285 other samples.

286 The absorption peaks at 1480, 1400, and 880 cm⁻¹ correspond to CO₃²⁻ on PO₄³⁻ sites, suggesting
287 that all the samples are slightly carbonated. Carbonation of HA commonly occurs unless
288 measures are taken to specifically exclude CO₂/CO₃²⁻ from the synthesis. These results are
289 coherent with TGA data reported forward in the text.

290 The Raman spectrum collected on HAp powder heated at 700°C is used as reference to evaluate
291 the impact of increasing Ti content on the Raman spectra acquired on the thermally treated
292 TiHAs and are presented in Fig. 3. Different spectral regions displaying characteristic signals
293 of HA (945-980 cm⁻¹, Fig. 3a) and TiO₂ (80-250 cm⁻¹ and 300-850 cm⁻¹), respectively, are

294 magnified in Fig. 3b and 3c for each of the synthesized samples. The prominent band seen at
295 $\sim 963\text{ cm}^{-1}$ is ascribed to the ν_1 PO_4 stretching mode of HA. Careful analysis of the ν_1 band
296 indicates a small asymmetry on the lower wavelength side, which is due to a signal occurring
297 at $\sim 955\text{-}957\text{ cm}^{-1}$. This could be ascribed to the presence of small amounts of poorly crystalline
298 carbonated apatite and/or amorphous calcium phosphate. The mean position and full width at
299 half maximum of the principal HA band as determined from the peak decomposition is \sim
300 $963.5 \pm 0.5\text{ cm}^{-1}$ and $\sim 6 \pm 0.3\text{ cm}^{-1}$ respectively. These are typical values reported in the literature
301 for the ν_1 phosphate mode in HA.⁴⁵

302 Five Raman bands that are not present in the spectrum of HAp can be clearly observed in the
303 spectra of all the TiHAs in Fig. 3b and 3c. These bands are found at 145, 197, 399, 518 and 640
304 cm^{-1} in excellent agreement with the Raman bands typically reported for anatase.⁴⁶ The doubly
305 degenerate mode at 145 cm^{-1} is the strongest band for the anatase phase and it is conveniently
306 used to investigate the evolution of TiO_2 as a function of titanium ion substitution in the apatite
307 lattice. The area of this absorption band determined by its systematic fitting performed for all
308 the TiHAs increases exponentially with the increasing concentration of Ti (Fig. 3d), in
309 accordance with the higher amount of TiO_2 already detected by the analysis of XRD profiles
310 collected on thermally treated TiHAs.

311 3.5 Chemical composition and structure of TiHA nanoparticles

312 The bulk chemical compositions determined from ICP-OES analysis of the as-synthesized
313 TiHAs are reported in Table 3, together with the carbonation extent evaluated by the
314 thermogravimetric analysis (TGA) as the weight loss occurring between $550\text{ }^\circ\text{C}$ and $950\text{ }^\circ\text{C}$.
315 The amounts of titanium detected and nominally introduced during the synthesis are in a good
316 agreement. The Ca/P molar ratio in all of the TiHAs is higher with respect to that of pure HAp,
317 the highest value being recorded for TiHA17. The Ca/P ratio displayed by this latter sample is

318 significantly higher respect to those displayed by the other TiHAs which instead feature similar
319 values.

320 The (Ti+Ca)/P molar ratio increases as expected with increasing concentrations of titanium, but
321 this relation is not linear, being the value of TiHA17 higher than that of TiHA25. Interestingly,
322 the Ca/(P+Ti) molar ratios detected for TiHA8 and TiHA17 are close to the Ca/P value of HAp,
323 while those of TiHA25 and TiHA50 are much smaller and deviate significantly from it. At this
324 regard, it is important to notice that carbonation occurred with similar extent ($\text{CO}_3^{2-} < 2 \text{ wt}\%$)
325 in all of the synthesis.

326 An increasing trend of the SSA values with increasing titanium concentrations is recorded, but
327 differences are only relevant when comparing TiHAs with a high amount (TiHA25 and
328 TiHA50) with those with a short amount of Ti (TiHA8 and TiHA17), for which the highest and
329 the lowest SSA values have been respectively determined (the lowest values being determined
330 for HAp). On the other hand, after thermal treatment at 700°C the SSA of all the powders
331 dropped to values around $20 \pm 2 \text{ m}^2/\text{g}$. Such an evident decrease is a well-known effect caused
332 by the densification of HA accompanied by grain growth induced by the thermal annealing.

333 TEM analysis of the samples reveals that Hap is composed of NPs having well defined rod-like
334 morphologies (Fig. 4a), with lengths typically in the 100 – 300 nm size range and widths of
335 about 20 – 50 nm in good agreement with the XRD and HR-PXRD analysis. On the contrary,
336 TiHAs NPs are observed as agglomerates of rounded, platelet-like morphologies (Fig. 4b-e).
337 All samples exhibit primary particle dimensions of 100 – 200 nm, regardless of the amounts of
338 titanium introduced during their synthesis. Very small crystallites ($< 20\text{nm}$) are occasionally
339 observed only on TiHAs at high Ti concentrations. At this regard, it is reported in the literature
340 that the fast hydrolysis of titanium isopropoxide precursor generates amorphous TiO_2
341 nanorods,⁴⁷ that however are not observed on TiHAs.

342 Porosity is detected in all the samples, including the unmodified HAp NPs magnified together
343 with TiHA50 NPs in Fig.5a and 5b respectively, with nanopores having typical dimensions of
344 < 20 nm as observed in some but not all of the rods and platelets.

345 The collected selected area electron diffraction patterns (SAED) reported in the insets in Fig.
346 4a-e reveal the occurrence of crystalline HA as the main phase of all the samples, but unassigned
347 spots/rings suggest the presence of a secondary phase which is tentatively assigned to the
348 occurrence of calcium titanium phosphate as already reported by HR-PXRD.

349 3.6 Polypyrrole coating on wool yarns

350 SEM pictures of bare natural wool fibers, WAP and WAEP5 are depicted in Fig. S4a-d, together
351 with a scheme representing a transversal section of wool yarns coated with a PPy layer doped
352 with ADA and PyE (Fig. S4a, dopant molecules are not accurately positioned in the scheme).

353 A change in surface morphology is observable starting from natural wool (Fig. S4b) to WAP
354 fibers (Fig. S4c) that becomes rugged and features the occurrence of small round shaped
355 particles of PPy. The surface roughness is further increased in WAEP (Fig. S4d) by the addition
356 of 5 mol% of PyE, resulting in the formation of bigger round particles of PPy with a diameter
357 around 1 μm . The resistivity of PPy coated fibers is found to be of a few $\text{k}\Omega / \text{cm}$ (Table S3),
358 some units lower than those already reported in the literature for related PPy-coated synthetic
359 fibers,⁴⁸ with a sensible increase of conductivity for the PPy doped with both ADA and PyE .
360 No changes in the fiber surface morphology (picture not shown), nor further resistance
361 reductions or increase in the mineralization extent (data reported below) could be observed with
362 the increasing concentration of PyE from 5 up to 10 mol% of PPy for WAEPs fibers.

363 3.7 Mineralization of PPy-conductive wool yarns with TiHA

364 SEM pictures at increasing magnification of WAP, WAEP5 and WAEP10 fibers mineralized
365 with TiHA25 are presented in Fig. 6a-b, 6c-d and 6e-f respectively.

366 No differences in the TiHA25 coating extent nor in the nanoparticles morphology can be
367 observed from the SEM pictures collected on mineralized WAEP5 and WAEP10 reported in
368 Fig.6c-d and Fig.6e-f respectively, both presenting only a few bare areas on their surface which
369 is largely covered by a layer of NPs deposited during the mineralization process.

370 On the other hand, mineralization experiments carried out on WAP produce fibers poorly coated
371 with TiHA25 NPs with a similar surface morphology compared to that of unmineralized fibers,
372 and reported respectively in Fig. 6a and Fig. S4c.

373 Higher magnification SEM imaging shows the presence of rod-like NPs – with morphologies
374 and dimensions very close to those determined by TEM analysis on TiHAs samples – covering
375 only the surface of WAEPs fibers (Fig. 6d and 6f), while the PPy covering the WAP fibers is
376 still visible after the mineralization (Fig. 6b).

377 The bottom phase precipitated during the mineralization experiments was analyzed by XRD
378 (data not showed) and displays a diffraction profile identical to that collected on TiHA25 for
379 both WAP and WAEPs. To further assess the similarity between the TiHA25 synthesized and
380 that mineralized on WAEPs fibers, the semiconductor layer was manually separated by the
381 fibers to be ground, sieved and analyzed as already described for synthesized TiHAs. The data
382 collected on the resulting samples are in perfect agreement with those already described for
383 TiHA25 powder, and thus are not reported further in the text to avoid data redundancy.

384 SEM pictures of knotted bare and mineralized WAEP5 yarns subjected to 10 stretching/release
385 cycles are depicted respectively in Fig.7a and 7b, together with a picture of a WAEP5 fiber
386 mineralized with TiHA25 after dipping in ethanol in Fig. 7c. No significant difference was
387 noticed by comparing the flexibility of unmineralized and mineralized WAEP5 yarns, with the
388 latter retaining both the semiconductor coating and WAEPs yarns original deformability.

389 Finally, the semiconductor coating was not altered by the dipping in ethanol and conserved the
390 original extension and morphology of mineralized WAEP5 fibers.

391 **4. Discussion**

392 4.1 TiHA physicochemical characterization

393 During the synthesis of the TiHAs titanium ions replace phosphate groups instead of calcium
394 in the HA lattice giving powders with suitable photo-electrical properties for application as
395 wide band gap semiconductors in flexible electronics, e.g. like photoanodes in DSC cells. The
396 obtained powders have higher SSAs (101-146 m²/g) with respect to those typically reported for
397 conventional DSC semiconductors (30-80 m²/g), and considering that high-performance
398 photoanodes require a large surface area for dye adsorption, these results show that calcium-
399 phosphate based photoanodes can potentially take up significantly more dye molecules
400 compared to conventional ones (i.e. ZnO and TiO₂). One of the key factors determining such
401 high SSAs is the nanoporosity, as it can be observed by the TEM pictures reported in Fig. 5a,b
402 due to the isopropanol used during the synthesis. The pores are then formed by the incorporation
403 of the titanium precursor as part of the reaction mixture which is trapped inside the forming
404 NPs and then removed due to evaporation.

405 The elemental composition of TiHAs shows that the doping ions are completely or partially
406 incorporated into hydroxyapatite lattice during the synthesis, as a variation of the Ca/P molar
407 ratio from that recorded on pure HAp is detected and moreover as the increase of Ti from 0 to
408 17 molar % relative to P is followed by a rapid increase of the Ca/P molar ratio, corresponding
409 to a phosphorous depletion or at least to a calcium enrichment, while the (Ti+Ca)/P molar ratio
410 increases up to values not compatible with the substitution of Ca with Ti ions in the apatite
411 structure. On the other hand, the Ca/(P+Ti) molar ratios of TiHA8 and TiHA17 are close to the
412 Ca/P ratio of reference HAp, suggesting more phosphorus than calcium replacement by
413 titanium ions in the apatite structure.

414 This result is reinforced by the XRD analyses performed on thermally treated powders showing
415 an increased crystallinity of the HA phase and the formation of β -TCP - which occurred for all

416 the powders with the exception of HAp - due to the instability of the titanium-modified apatitic
417 phase. In this regard, Raynaud et al. showed that HA with a Ca/P ratio lower than that of
418 stoichiometric HA (1.67) start to decompose into β -TCP when heated in air at 700°C.⁴⁹ Thus,
419 the thermal decomposition of TiHAs into triphasic mixtures of HA, β -TCP, and anatase is
420 consistent with a deviation from the Ca/P molar ratio compared to that of HAp (for which no
421 β -TCP was observed) due to the successful introduction of titanium in the apatite lattice.
422 However, the data reported in the present study are only in partial agreement with what reported
423 by Raynaud, as the formation of β -TCP from the TiHAs synthesized in this study appears to be
424 related to a phosphorus rather than a calcium deficiency of the TiHA.

425 Anatase is absent in thermally treated HAp and TiHA8 and is produced only in small amounts
426 during the thermal treatment of sample TiHA17, while large amounts of this phase are formed
427 during the thermal decomposition of TiHA25 and TiHA50. The presence of perovskite
428 (CaTiO_3), which was previously reported to be formed under calcination of titanium HAs,⁵⁰ is
429 excluded instead for all the samples, but signals ascribable to an additional phase, probably
430 $\text{CaTi}_4(\text{PO}_4)_6$, were detected from the HR-PXRD analysis of TiHA8 and especially of TiHA50.
431 However, the identity of this phase could not be unambiguously assigned due to the low S/N
432 ratio and the low number of peaks.

433 Also the TEM and the SAED analyses reveal the occasional presence of a secondary phase
434 consisting of round shaped aggregated of very small crystallites (< 20 nm), especially in the
435 cases of TiHA25 and TiHA50 NPs for which only partial substitution by titanium ions has
436 occurred. The presence of such a secondary phase, which is likely to be amorphous TiO_2 , could
437 be one of the factors determining the slightly larger surface areas of TiHA25 and TiHA50 with
438 respect to TiHA8 and TiHA17.

439 It is worth noting that the titanium precursor used during the synthesis is a titanium alkoxide
440 with small alkyl chains and that both these features comply with a fast hydrolysis kinetic due

441 to the easiness with which the Ti coordination sites occupied by alkyl chains are hydrolyzed.⁵¹
442 Sol-gel synthesis of TiO₂ by fast hydrolysis of titanium alkoxide precursor carried out at low
443 temperature give amorphous titanium dioxide NPs,⁵² that upon thermal treatment can be
444 converted into crystalline anatase⁵³ corroborating the hypothesis of amorphous TiO₂ formation
445 during the synthesis of TiHA.

446 The occurrence of amorphous TiO₂ only for Ti concentration values above 17 molar % with
447 respect to P can be explained by the preferential substitution of PO₄³⁻ with oxy/hydroxy anions
448 of Ti (i.e. ions with a general formula H_xTiO_y^{4+x-2y}) up to this Ti/P molar ratio - that is to say,
449 up to a value of 10% for the Ti/Ca ratio. Above this concentration the excess of titanium
450 precursor is oxidized to amorphous TiO₂. Such mechanism is in partial agreement with what
451 reported by Tsukada et al. who described the formation of particles of amorphous titanium
452 phosphate through the synthesis of titanium-modified HA, when the titanium concentration
453 Ti/(Ca+Ti) exceeded 10%, hypothesizing the one-to-one substitution of Ca²⁺ with Ti⁴⁺.⁷

454 The data presented in this work provides strong evidence that Ti⁴⁺ ions replace PO₄³⁻, but even
455 if the decrease of the Bragg factor relative to the Rietveld refinement of the HR-PXRD pattern
456 of TiHA50 suggests the substitution of phosphate by titanate ions, similarly to what is already
457 described on sintered TiHAs in the litterature,⁵⁴ it was not possible to assure whether phosphates
458 is substituted by titanate, titanium oxy/hydroxide, or other titanium anions in the apatitic lattice.

459 On the other hand, the replacement of PO₄³⁻ instead of Ca²⁺ by titanium doping is in contrast to
460 the theoretical calculation for Ti-substituted HA reported by Yin et al. using density functional
461 theory, where only the occurrence of [Ti(OH)_x]^{4-x} ions - with x ranging from 0 to 2 - was
462 considered in place of calcium, excluding phosphates from the calculations.⁵⁴ Ti⁴⁺ has a smaller
463 atomic radius and a higher valence respect to Ca²⁺ (0.074 nm and 0.110 nm respectively for 6-
464 coordinate Ti⁴⁺ and 6-coordinate Ca²⁺ respectively), thus their direct interchange seems unlikely
465 unless the titanium precursor introduced during the synthesis oxidizes to generate [Ti(OH)_x]^{4-x}

466 ions with a larger molecular radius and a charge similar to that of Ca^{2+} . However, several studies
467 reported assert that the direct substitution of Ca^{2+} with Ti^{4+} is a possible pathway.^{15,16,54,55,56}
468 For instance, Anmin et al.⁵⁵ attributes the decrease of HAp cell volume to a direct Ca^{2+}
469 replacement with Ti^{4+} , while other studies suggest that titanium can replace calcium only as a
470 divalent ionic group, that is to say as $[\text{Ti}(\text{OH})_2]^{2+}$ and/or $[\text{Ti}(\text{HPO}_4)]^{2+}$.^{15,16} This substitution
471 mechanism is also supported by two further publications, one on the manufacturing of TiHA
472 by ionic exchange through a dissolution/precipitation mechanism in the presence of a divalent
473 titanium precursor,⁵⁶ and the other on the computational calculations carried out on TiHA which
474 reports a strong preference for $\text{Ti}(\text{OH})_2^{2+}$ occupancy on Ca(2) site up to a Ti/Ca 10 % ratio.⁵⁴
475 Nevertheless, in this work we report that titanium actually replaces phosphorous up to Ti/P 17
476 molar %, while above this concentration a secondary phase probably consisting of round
477 aggregates of small crystallites of amorphous TiO_2 starts to occur. This phase is not identifiable
478 by XRD analysis but could be occasionally detected by TEM as NPs in TiHA25 and TiHA50,
479 and indirectly as anatase from the XRD profiles and from the Raman spectra of thermally
480 treated powders.

481 Regardless of the amount of doping ions introduced during the synthesis, the band gap value of
482 HA is sensibly moved towards a suitable band gap range for application in photoactive devices
483 by titanium doping. The recorded values are in perfect agreement with those reported by
484 Tsukada et al.,⁷ despite the fact that, as already mentioned, he attributes the introduction of Ti
485 into the HA lattice to Ca instead of P substitution.

486 As a result of the optimized band gap energy, SSA and microstructure compared to the samples
487 with lower Ti content we selected sample TiHA25 for mineralization experiments on WAP and
488 WEAPs yarns. TiHA25 was also preferred to TiHA50 for the better dispersion of its NPs in
489 water suspension, as evidenced by the lower Z-average value and its hydrodynamic diameter

490 distribution, all being important factors for the mineralization process affecting the
491 homogeneity of fiber surface coating.

492 4.2 Bio-inspired mineralization of TiHA on polypyrrole coated wool fibers

493 The successful nucleation of TiHA25 on PPy-coated conductive wool fibers provides a proof
494 of concept for the assembly of fabric integrated electronic devices through two simple processes
495 like oxidative polymerization of PPy and TiHA controlled bio-inspired mineralization. A
496 pivotal role in the deposition of TiHA on the conductive wool yarns is played by the doping of
497 the PPy coating with PyE that modifies the physicochemical properties of the PPy layer by
498 increasing its wettability, and promotes the nucleation of TiHA25 on its surface by means of
499 its carboxyl group.

500 Without PyE molecules, PPy-coated wool fibers are much more hydrophobic and more
501 importantly TiHA25 could not be mineralized on their surfaces. In this regard, it is worthy to
502 note that PyE was chosen as dopant not only because of its similarity to the pyrrole molecules
503 – as can be seen from the scheme in Fig. S4a – but also because it displays a carboxylic moiety.
504 In this respect, Toworfe G.K. et al.⁵⁷ demonstrated that carboxylic modified surfaces are more
505 hydrophilic than those modified with amines and hydroxyls, in accordance with the increased
506 wettability of the PPy-coated fibers observed during the mineralization of TiHA25. Moreover,
507 compounds containing the carboxyl or amine functional group are largely reported to foster the
508 adsorption and crystallization of calcium phosphates,⁵⁸⁻⁶⁰ as in the case of collagen molecules,
509 whose carboxylate moieties are supposed to be responsible for the nucleation of HA NPs on
510 collagen from SBF solution.^{61,62}

511 The introduction of PyE in PPy considerably increases TiHA25 deposition on the PPy-coated
512 wool fibers, and surprisingly its introduction prompts an increase of conductivity of the PPy
513 layer. No differences are observable by doubling the amount of PyE, i.e. passing from a
514 PyE/pyrrole ratio of 5 mol% to a 10 mol%, for both the increased TiHA NPs mineralization

515 and PPy raise of conductivity. On the other hand, the combination of ADA and PyE results in
516 a further increase of conductivity, but whether this additional conductivity raise is due to the
517 intrinsic property of PyE or to the augmented quantities of PPy deposited on the fiber surface
518 cannot be unambiguously decided, as the introduction of PyE is likely to cause both the effects.
519 Also, the PPy conductivity is largely affected by the increased overall layer thickness.⁶³
520 As we have shown, the electrical resistivity of the PyE-doped PPy layers is promising for
521 functional and flexible electronic devices. There is evidence provided by J. Wu et al.⁶⁴ who
522 report significantly better values for conductive layers made of this organic polymer,
523 demonstrating that a further improvement of its conductivity performance can be achieved in
524 the future. Our studies show that PyE prompts the nucleation of rod-like TiHA nanocrystals
525 retaining the chemical composition, morphology, SSA and band gap values of the parental
526 TiHA powders, proving the applicability of bio-inspired approach for the obtainment of fiber-
527 shaped optoelectronic flexible devices. On the contrary, WAP fibers were not successfully
528 covered by TiHA25 during the mineralization process, with only a small deposition of mineral
529 phase on some areas of its surface.

530 The nanometric size of the semiconductor layer is probably the principal factor determining the
531 retention of WAEPs yarns deformability after TiHA25 mineralization that would be lost in case
532 of the deposition of coarser grains as induced by the thermal treatment of TiHAs. Thus,
533 even if it is well known that the physicochemical and properties of HA can be optimized
534 by thermal annealing, this will also determine the formation of a brittle ceramic layer
535 limiting the flexibility of the fiber and eventually facilitating its peeling-off from the
536 conductive PPy layer. Moreover, the high SSA displayed by TiHAs semiconductor layer
537 would be impaired by the thermal treatment determining its remarkable reduction up to
538 the 85% of the original. A large SSA is in fact a highly desirable feature in wide band gap
539 semiconductors that could be exploited *e.g.* by adsorbing dye molecules onto them to

540 increase their photoelectric performances. An easy way to achieve the incorporation of
541 dyes in semiconductors is by dipping them into an organic solvent. At this regard, the
542 TiHA layer mineralized on the surface of WAEP5 fibers endured to a simulated dipping
543 process into ethanol at 40°C, preserving its extension and adhesion on the PPy layer.
544 To the best of our knowledge, no work reporting the mineralization of HA, nor of other calcium
545 phosphates on PPy is present in the literature, even though numerous works report the coating
546 of this highly conductive polymer using TiO₂,⁶⁵ ZnO,²¹ other metallic oxides and materials like
547 carbon nanotubes.^{22,23,65}
548 One of the key challenges in the future is the retention of fiber flexibility after semiconductor
549 deposition. For this purpose we aim to develop a procedure using a protective layer, or by an
550 electrolyte and a redox mediator in the case of a flexible fiber-shaped DSCs device.⁶⁶

551

552 **5. Summary and Conclusions**

553 Four hydroxyapatite based samples modified with increasing amounts of titanium were
554 successfully obtained and their suitability to work as semiconductors in flexible electronic
555 devices was evaluated by measuring their physico-chemical properties, paying particular
556 attention to their band gap values and their SSAs.

557 During their precipitation, titanium was found to replace phosphorous in the apatite lattice up
558 to Ti/P 17% molar ratio, with the occasional formation of negligible amounts of CaTi₄(PO₄)₆,
559 while the excess of doping ions was rapidly oxidized to amorphous titanium dioxide.

560 Optimized properties were identified for a 25 molar% of Ti/P, corresponding to a Ti/Ca content
561 of 15 molar%. This material was deposited onto the surface of conductive wool yarns produced
562 by in situ chemical oxidative polymerization of pyrrole directly on the fibers surface. This step
563 was made possible by the doping of the resulting polypyrrole layer with anthraquinone-2-
564 sulfonic acid, used to enhance the electric conductivity, and pyroglutamic acid which rendered

565 more hydrophilic the conductive layer and, thanks to its carboxylic moiety, drove the nucleation
566 of apatite on the polypyrrole surface.

567 In conclusion, this work reports the successful production through simple processes like
568 oxidative polymerization and mineralization, of a concentric fiber-shaped building block
569 designed for flexible optoelectronic devices and consisting of a layer of titanium-modified HA
570 (wide band gap semiconductor) nucleated on a layer of polypyrrole (conductive layer)
571 supported by wool natural fibers, that may find useful applications in radiation sensors,
572 photocatalytic devices and wearable electronics.

573

574 **Acknowledgements**

575 This work was supported by the European Union 7th Framework Program under the Grant
576 Agreement n°310637 SMILEY. We thank Diamond Light Source for access to the High
577 Resolution Powder Diffraction beamline I11. Pierre GRAS would like to thank INP Toulouse
578 for the financial support of his 1 month secondment in Italy. This research is supported by the
579 ANR “Agence Nationale de la Recherche” (ref: Innov’Hap: ANR-12-BS09-0030) and “Region
580 Midi-Pyrenées” (CLE n°12052853).

References

- [1] M. Caironi; T.D. Anthopoulos, Y.Y. Noh, J. Zaumseil, Organic and hybrid materials for flexible electronics. *Adv Mat.* 2013, **25**, 4208-4209.
- [2] S Akhtar, M.S. Alghamdi, Y.G. Malik, M.A. Khalil, R.M.A. Riaz, S. Naseem, Structural, optical, magnetic and half-metallic studies of cobalt doped ZnS thin films deposited via chemical bath deposition. *J. Mater. Chem. C*, 2015, **3**(26), 6755-6763.
- [3] M.Y Yen, M.C. Hsiao, S.H. Liao, P.I Liu, H.M Tsai, C.C.M. Ma, N.W. Pu, M.D. Ger, Preparation of graphene/multi-walled carbon nanotube hybrid and its use as photoanodes of dye-sensitized solar cells. *Carbon.*, 2011, **49**, 3597-3606.
- [4] J. Zhang, W. Peng, Z. Chen, H. Chen, L. Han, Effect of cerium doping in the TiO₂ photoanode on the electron transport of dye-sensitized solar cells. *J. Phys. Chem. C*, 2012, **116**, 19182-19190.
- [5] Y. Duan, N. Fu, Q. Liu, Y. Fang, X. Zhou, J. Zhang, Y. Lin, Sn-doped TiO₂ photoanode for dye-sensitized solar cells. *J. Phys. Chem. C*, 2012, **116**, 8888-8893.
- [6] A. Latini, C. Cavallo, F.K. Aldibaja, D. Gozzi, D. Carta, A. Corrias, L. Lazzarini, G. Salviati, Efficiency improvement of DSSC photoanode by scandium doping of mesoporous titania beads. *J. Phys. Chem. C*, 2013, **117**, 25276-25289.
- [7] M. Tsukada, M. Wakamura, N. Yoshida, T. Watanabe, Band gap and photocatalytic properties of Ti-substituted hydroxyapatite: Comparison with anatase-TiO₂. *J. Mol. Catal. A-Chem.*, 2011, **338**, 18-23.
- [8] X. Wang, Y Sun, K. Lin, Facile synthesis of dental enamel-like hydroxyapatite nanorod arrays via hydrothermal transformation of hillebrandite nanobelts. *J. Mater. Chem. B*, 2015, **3**(37), 7334-7339.
- [9] Z. Wei, C. Xu, B. Li, Application of waste eggshell as low-cost solid catalyst for biodiesel production. *Bioresource Technol.*, 2009, **100**, 2883-2885.
- [10] M. Uota, H. Arakawa, N. Kitamura, T. Yoshimura, J. Tanaka, T. Kijima, Synthesis of high surface area hydroxyapatite nanoparticles by mixed surfactant-mediated approach. *Langmuir*, 2005, **21**, 4724-4728.
- [11] Y.P. Guo, T. Long, S. Tang, Y.J. Guo, Z.A. Zhu. Hydrothermal fabrication of magnetic mesoporous carbonated hydroxyapatite microspheres: biocompatibility, osteoinductivity, drug delivery property and bactericidal property. *J. Mater. Chem. B*, 2014, **2**(19), 2899-2909.
- [12] M. Iafisco, C. Drouet, A. Adamiano, P. Pascaud, M. Montesi, S. Panseri, S. Stephanie, A. Tampieri, Superparamagnetic iron-doped nanocrystalline apatite as a delivery system for doxorubicin. *J. Mater. Chem. B*, 2016, **4**(1), 57-70.
- [13] V. Iannotti, A. Adamiano, G. Ausanio, L. Lanotte, G. Aquilanti, J.M.D. Coey, M. Lantieri, G. Spina, M. Fittipaldi, G. Margarisi, K. Trohidou, S. Sprio, M. Montesi, S. Panseri, M. Sandri, M. Iafisco, A. Tampieri. Fe-Doping-Induced Magnetism in Nano-Hydroxyapatites. *Inorg. Chem.*, 2017, **56**(8), 4446-4458.
- [14] Y. Liu, H. Zhong, L. Li, C. Zhang, Temperature dependence of magnetic property and photocatalytic activity of Fe₃O₄/hydroxyapatite nanoparticles. *Mater. Res. Bull.*, 2010, **45**, 2036-2039.
- [15] M. Nishikawa, W. Yang, Y. Nosaka, Grafting effects of Cu²⁺ on the photocatalytic activity of titanium-substituted hydroxyapatite. *J of Mol Catal A-Chem.*, 2013, **378**, 314-318.

- [16] M. Wakamura, K. Hashimoto, T. Watanabe, Photocatalysis by calcium hydroxyapatite modified with Ti (IV): albumin decomposition and bactericidal effect. *Langmuir*, 2003, **19**, 3428-3431.
- [17] K. Kandori, T. Kuroda, M. Wakamura, Protein adsorption behaviors onto photocatalytic Ti(IV)-doped calcium hydroxyapatite particles, *Colloids Surf. B.*, 2011, **87**, 472–479.
- [18] C.C. Ribeiro, M.A. Barbosa, A.A.S.C. Machado, A. Tudor, M.C. Davies, Modifications in the molecular structure of hydroxyapatite induced by titanium ions. *J. Mater. Sci-Mater. M.*, 1995, **6**, 829-834.
- [19] A. Ślósarczyk, A. Zima, Z. Paszkiewicz, J. Szczepaniak, A.H. De Aza, A. Chróścicka, The influence of titanium on physicochemical properties of Ti-modified hydroxyapatite materials. *Materiały Ceramiczne /Ceramic Materials/*, 2010, **62**(3), 369-375
- [20] Z. Wang, Z. Xu, W. Zhao, N. Sahai. A potential mechanism for amino acid-controlled crystal growth of hydroxyapatite. *J. Mater. Chem. B*, 2015, **3**(47), 9157-9167.
- [21] C.A. Ferreira, S.C. Domenech, P.C. Lacaze, Synthesis and characterization of polypyrrole/TiO₂ composites on mild steel. *J. Appl. Electrochem.*, 2001, **31**, 49-56.
- [22] Y. Hao, M. Yang, W. Li, X. Qiao, L. Zhang, S. Cai, A photoelectrochemical solar cell based on ZnO/dye/polypyrrole film electrode as photoanode. *Sol. Energ. Mat. Sol. C.*, 2000, **60**, 349-359.
- [23] J. Zhang, S. Wang, M. Xu, Y. Wang, H. Xia, S. Zhang, X. Gou, S. Wu, Polypyrrole-coated SnO₂ hollow spheres and their application for ammonia sensor. *J. Phys. Chem. C.*, 2009, **113**, 1662-1665.
- [24] E.P. Scilingo, F. Lorussi, A. Mazzoldi, D. De Rossi, Strain-sensing fabrics for wearable kinaesthetic-like systems. *IEEE Sens. J.*, 2003, **3**, 460.
- [25] F. Lorussi, W. Rocchia, E.P. Scilingo, A. Tognetti, D. De Rossi, Wearable, redundant fabric-based sensor arrays for reconstruction of body segment posture. *IEEE Sens. J.*, 2004, **4**, 807.
- [26] Y. Li, G. Shi. Electrochemical growth of two-dimensional gold nanostructures on a thin polypyrrole film modified ITO electrode. *J. Phys. Chem. B.*, 2005, **109**, 23787-23793.
- [27] L. Vayssieres, Growth of arrayed nanorods and nanowires of ZnO from aqueous solutions. *Adv. Mat.*, 2003, **15**, 464-466.
- [28] J. Rodríguez-Carvajal, Recent Developments of the Program FULLPROF, Commission on Powder Diffraction (IUCr) Newsletter, 2001, 26, 12-19.
- [29] N. Sangiorgi, L. Aversa, R. Tatti, R. Verucchi, A. Sanson, Spectrophotometric method for optical band gap and electronic transitions determination of semiconductor materials. *Opt. Mater.*, 2017, **64**, 18-25.
- [30] N.C. Popa, The (hkl) Dependence of Diffraction-Line Broadening Caused by Strain and Size for All Laue Groups in Rietveld Refinement. *J. Appl. Cryst.*, 1998, **31**, 176-180
- [31] M. Iafisco, B. Palazzo, G. Martra, N. Margiotta, S. Piccinonna, G. Natile, V. Gandin, C. Marzano, N. Roveri, Nanocrystalline carbonate-apatites: role of Ca/P ratio on the uptake and release of anticancer platinum bisphosphonates. *Nanoscale*, 2012, **4**, 206-217.
- [32] A. Adamiano, D. Fabbri, G. Falini, M.G. Belcastro, A complementary approach using analytical pyrolysis to evaluate collagen degradation and mineral fossilisation in archaeological bones: The case study of Vicenne-Campochiaro necropolis (Italy). *J. Anal. App. Pyrol.*, 2013, **100**, 173-180.

- [33] M. Iafisco, E. Varoni, E. Battistella, S. Pietronave, M. Prat, N. Roveri, L. Rimondini, The cooperative effect of size and crystallinity degree on the resorption of biomimetic hydroxyapatite for soft tissue augmentation. *Int. J. Artif. Organs.*, 2010, **33**, 765–774.
- [34]. X. Huang, Z. Yu, S. Huang, Q. Zhang, D. Li, Y. Luo, Q. Meng, Preparation of fluorine-doped tin oxide (SnO₂:F) film on polyethylene terephthalate (PET) substrate, *Mater. Lett.*, 2010, **64**, 1701–1703.
- [35] R. Xu, J. Wei, F. Guo, X. Cui, T. Zhang, H. Zhu, K. Wang, D. Wu. Highly conductive, twistable and bendable polypyrrole–carbon nanotube fiber for efficient supercapacitor electrodes. *RSC Adv.*, 2015, **5**(28), 22015-22021.
- [36] R. Cruz-Silva, A. Morelos-Gomez, H.I. Kim, H.K. Jang, F. Tristan, S. Vega-Diaz, L.P. Rajukumar, A.L. Elías, N. Perea-Lopez, J. Suhr, M. Endo. Super-stretchable graphene oxide macroscopic fibers with outstanding knotability fabricated by dry film scrolling. *ACS nano*, 2014, **8**(6), 5959-5967.
- [37] C. J. Howard, T. M. Sabine, F. Dickson, Structural and thermal parameters for rutile and anatase, *Acta Cryst.*, 1991, **B47**, 462-468.
- [38] E. P. Meagher, G. A. Lager, Polyhedral thermal expansion in the TiO₂ polymorphs: refinement of the crystal structures of rutile and brookite at high temperature, *The Canadian Mineralogist*, 1979, **17**, 77-85.
- [39] M. Yashima, A. Sakai, T. Kamiyama, A. Hoshikawa, Crystal structure analysis of β -tricalcium phosphate Ca₃(PO₄)₂ by neutron powder diffraction, *J. Solid State Chem.*, 2003, **175**(2), 272-277.
- [40] P. F. Schofield, K.S. Knight K S, J. A. M. van der Houwen, E. Valsami-Jones, The role of hydrogen bonding in the thermal expansion and dehydration of brushite, di-calcium phosphate hydrate, *Phys. Chem. Miner.*, 2004, **31**, 606-624.
- [41] M. Catti, G. Ferraris, A. Filhol, Hydrogen bonding in the crystalline state. CaHPO₄ (monetite), P-1 or P1? A novel neutron diffraction study, *Acta Crystallogr.*, 1997, **B33**, 1223-1229.
- [42] W.E. Brown, Octacalcium phosphate and hydroxyapatite: crystal structure of octacalcium phosphate, *Nature*, 1962. **196**, 1048 – 1050.
- [43] A. Leclaire, A. Benmoussa, M. M. Borel, A. Grandin, B. Raveau, TiPO₄, a titanium orthophosphate with a CrVO₄ sublattice, *Eur. J. Solid State Inorg. Chem.*, 1991, **28**, 1323-1333.
- [44] P. Villars, *Material Phases Data System (MPDS)*, CH-6354 Vitznau, Switzerland (ed.) Springer Materials Ca_{0.5}Ti₂(PO₄)₃ (CaTi₄[PO₄]₆) Crystal Structure, http://materials.springer.com/isp/crystallographic/docs/sd_1621200.
- [45] G. Penel, G. Leroy, C. Rey, E. Bres, MicroRaman spectral study of the PO₄ and CO₃ vibrational modes in synthetic and biological apatites. *Calcif. Tissue Int.*, 1998, **63**(6), 475-481.
- [46] H.C. Choi, Y.M. Jung, S.B. Kim, Size effects in the Raman spectra of TiO₂ nanoparticles. *Vib. Spectrosc.*, 2005, **37**(1), 33-38.
- [47] P.D. Cozzoli, A. Kornowski, H. Weller, Low-temperature synthesis of soluble and processable organic-capped anatase TiO₂ nanorods. *J. Am. Chem. Soc.*, 2003, **125**, 14539-14548.
- [48] Y. Li, X.Y. Cheng, M.Y. Leung, J. Tsang, X.M. Tao, M.C.W. Yuen, A flexible strain sensor from polypyrrole-coated fabrics. *Synthetic Met.*, 2005, **155**, 89-94.

- [49] S. Raynaud, E. Champion, D. Bernache-Assollant, Calcium phosphate apatites with variable Ca/P atomic ratio II. Calcination and sintering. *Biomaterials*, 2002, **23**, 1073-1080.
- [50] C. Paluszkiwicz, J. Czechowska, A. Ślósarczyk, Z. Paszkiewicz, Evaluation of a setting reaction pathway in the novel composite TiHA–CSD bone cement by FT-Raman and FT-IR spectroscopy. *J. Mol. Struct.*, 2013, **1034**, 289-295.
- [51] D.D. Dunuwila, C.D. Gagliardi, K.A. Berglund, Application of controlled hydrolysis of titanium (IV) isopropoxide to produce sol-gel-derived thin films. *Chem. Mater.*, 1994, **6**, 1556-1562.
- [52] Z. Zhao, B.K. Tay, G. Yu. Room-temperature deposition of amorphous titanium dioxide thin film with high refractive index by a filtered cathodic vacuum arc technique. *Appl. Optics*, 2004, **43**, 1281-1285.
- [53] H. Zhang, M. Finnegan, J.F. Banfield, Preparing single-phase nanocrystalline anatase from amorphous titania with particle sizes tailored by temperature. *Nano Lett.*, 2001, **1**, 81-85.
- [54] S. Yin, D.E. Ellis. First-principles investigations of Ti-substituted hydroxyapatite electronic structure. *Phys. Chem. Chem. Phys.*, 2010, **12**, 156-163.
- [55] H. Anmin, L. Ming, C. Chengkang, M. Dali. Preparation and characterization of a titanium-substituted hydroxyapatite photocatalyst. *J. Mol. Catal. A-Chem.*, 2007, **267**, 79
- [56] C.C. Ribeiro, I. Gibson, M.A. Barbosa. The uptake of titanium ions by hydroxyapatite particles – structural changes and possible mechanisms. *Biomaterials*, 2006, **27**, 1749-1761.
- [57] G.K. Toworfe, R.J. Composto, I.M. Shapiro, P. Ducheyne. Nucleation and growth of calcium phosphate on amine-, carboxyl- and hydroxyl-silane self-assembled monolayers. *Biomaterials*, 2006, **27**, 631-642.
- [58] N. Spanos, P.G. Klepetsanis, P.G. Koutsoukos. Model studies on the interaction of amino acids with biominerals: the effect of L-serine at the hydroxyapatite–water interface. *J. Colloid Interf. Sci.*, 2001, **236**, 260-265.
- [59] W. Li, Y. Cai, Q. Zhong, Y. Yang, S.C. Kundu, J. Yao, Silk sericin microcapsules with hydroxyapatite shells: protection and modification of organic microcapsules by biomimetic mineralization. *J. Mater. Chem. B*, 2016, **4**(2), 340-347.
- [60] M. Tanahashi, T. Matsuda, Surface functional group dependence on apatite formation on self-assembled monolayers in a simulated body fluid. *J. Biomed. Mater. Res.*, 1997, **34**, 305-315.
- [61] R. Shahlori, G.I. Waterhouse, A.R. Nelson, D.J. Mc Gillivray, Morphological, chemical and kinetic characterisation of zein protein-induced biomimetic calcium phosphate films. *J. Mater. Chem. B*, 2015, **3**(30), 6213-6223.
- [62] S.H. Rhee, J.D. Lee, J. Tanaka, Nucleation of hydroxyapatite crystal through chemical interaction with collagen. *J. Am. Chem. Soc.*, 2000, **83**, 2890-2892.
- [63] A.C. Fou, M.F. Rubner, Molecular-level processing of conjugated polymers. 2. Layer-by-layer manipulation of in-situ polymerized p-type doped conducting polymers. *Macromolecules*, 1995, **28**, 7115-7120.
- [64] J. Wu, Q. Li, L. Fan, Z. Lan, P. Li, J. Lin, S. Hao. High-performance polypyrrole nanoparticles counter electrode for dye-sensitized solar cells. *J. Power Sources*, 2008, **181**, 172-176.
- [65] Y. Wang, W. Jia, T. Strout, A. Schempf, H. Zhang, B. Li, J. Cui, Y. Lei, Ammonia gas sensor using polypyrrole-coated TiO₂/ZnO Nanofibers. *Electroanal.*, 2009, **21**, 1432-1438.
- [66] S. Sahoo, G. Karthikeyan, G.C. Nayak, C.K. Das, Electrochemical characterization of in situ polypyrrole coated graphene nanocomposites. *Synthetic Met.*, 2011, **161**, 1713-1719.

Statement Contribution of Authors

Conception of the work:

Alessio Adamiano, Anna Tampieri, Alessandra Sanson

Design of the work:

Alessio Adamiano, Andrea Ruffini

Data collection:

Alessio Adamiano, Nicola Sangiorgi, Konstantinos Chatzipanagis, Matthew Bilton, Bartosz Marzec, Alessio Varesano.

Data analysis and interpretation:

Alessio Adamiano, Nicola Sangiorgi, Pierre Gras, Konstantinos Chatzipanagis, Alessio Varesano, Roland Kröger

Drafting the article:

Alessio Adamiano

Critical revision of the article:

Simone Sprio, Monica Sandri, Alessandra Sanson, David Grossin, Christine Francès, Fiona Meldrum, Roland Kroeger, Anna Tampieri

Final approval of the version to be published:

Alessio Adamiano, Nicola Sangiorgi, Simone Sprio, Andrea Ruffini, Monica Sandri, Alessandra Sanson, Pierre Gras, David Grossin, Christine Francès, Konstantinos Chatzipanagis, Matthew Bilton, Bartosz Marzec, Alessio Varesano, Fiona Meldrum, Roland Kröger, Anna Tampieri.

Conflict of interest

There are no conflicts of interest to declare

Figures

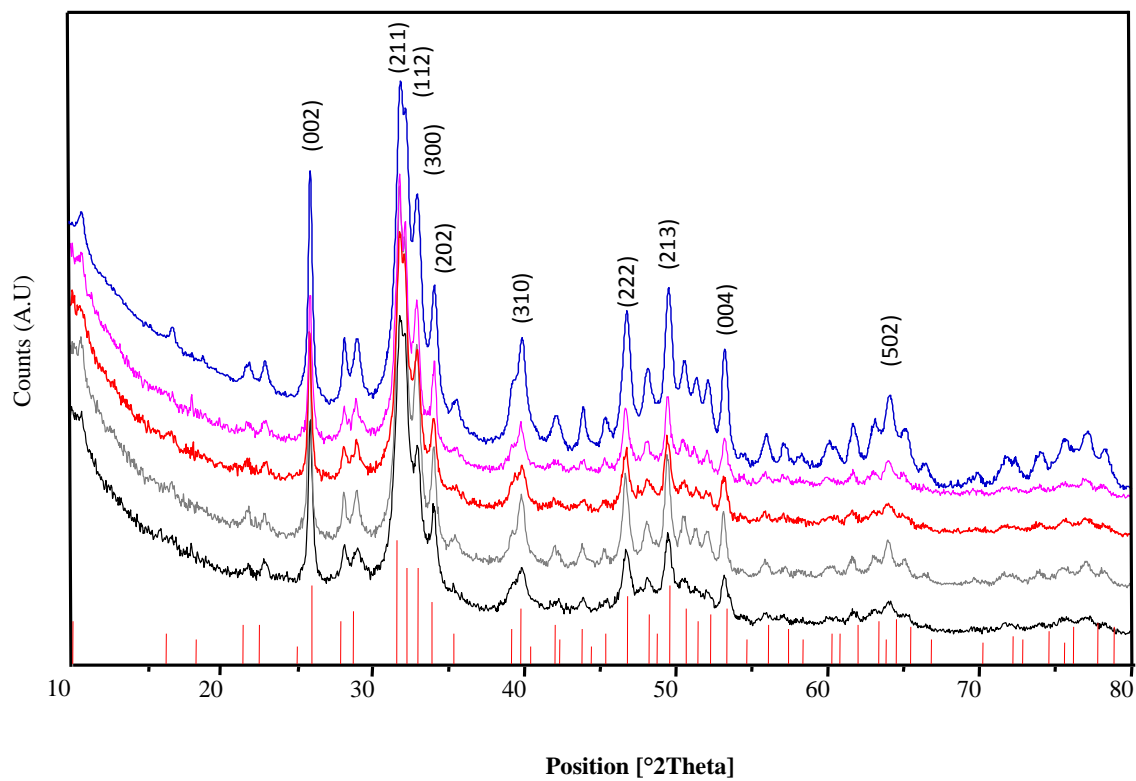


Figure 1. XRD diffraction patterns collected on (from the top to the bottom) HAp, TiHA50, TiHA25, TiHA17 and TiHA8.

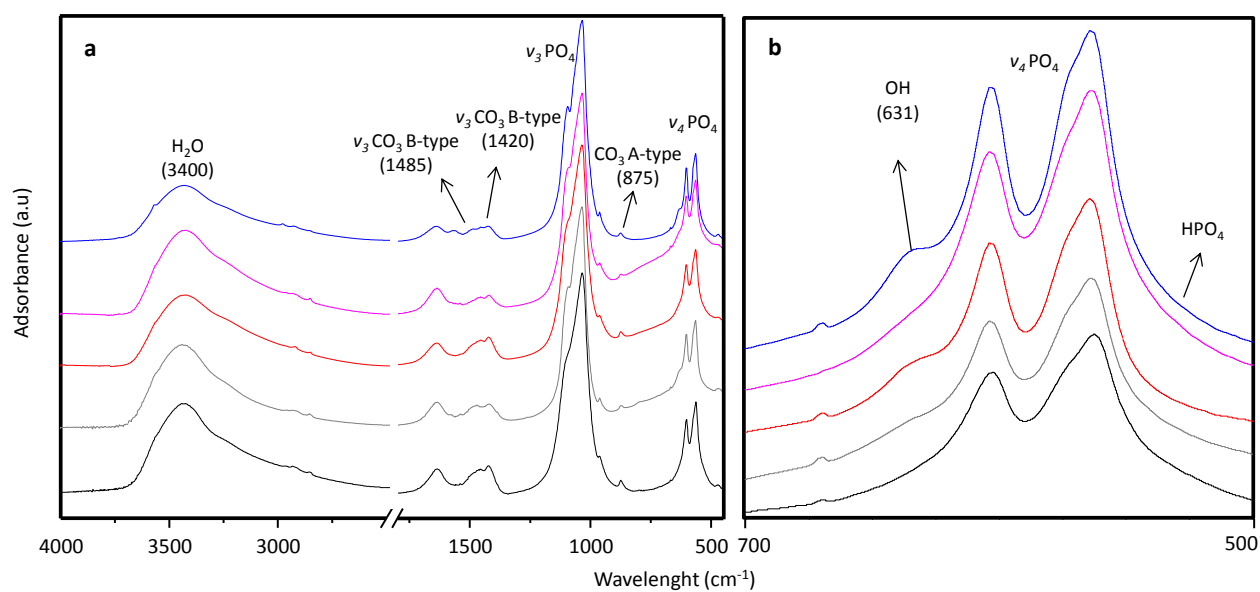


Figure 2. FT-IR spectra of (from the top to the bottom) HAp, TiHA50, TiHA25, TiHA17 and TiHA8 (a). Magnification of the FT-IR spectra in the region where the bands of $\nu_4\text{PO}_4$ (675–525 cm^{-1}) appeared (b).

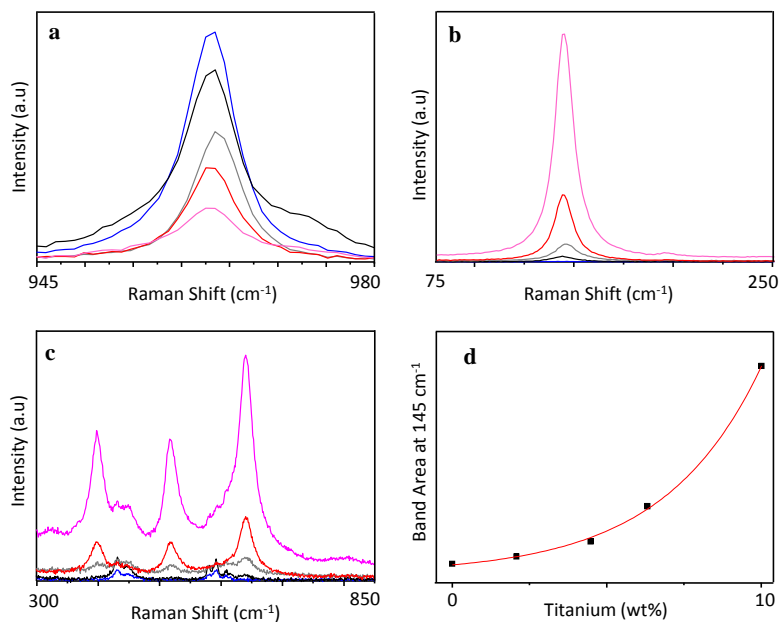


Figure 3. Evolution of the Raman bands of apatite (3a) and anatase (3b and 3c) of thermally treated HAp (blue), TiHA8 (black), TiHA17 (grey), TiHA25 (red), and TiHA50 (violet), together with the curve obtained by plotting the area of the Raman band at 145 cm^{-1} registered on all the TiHAs as a function of their Ti concentration (3d).

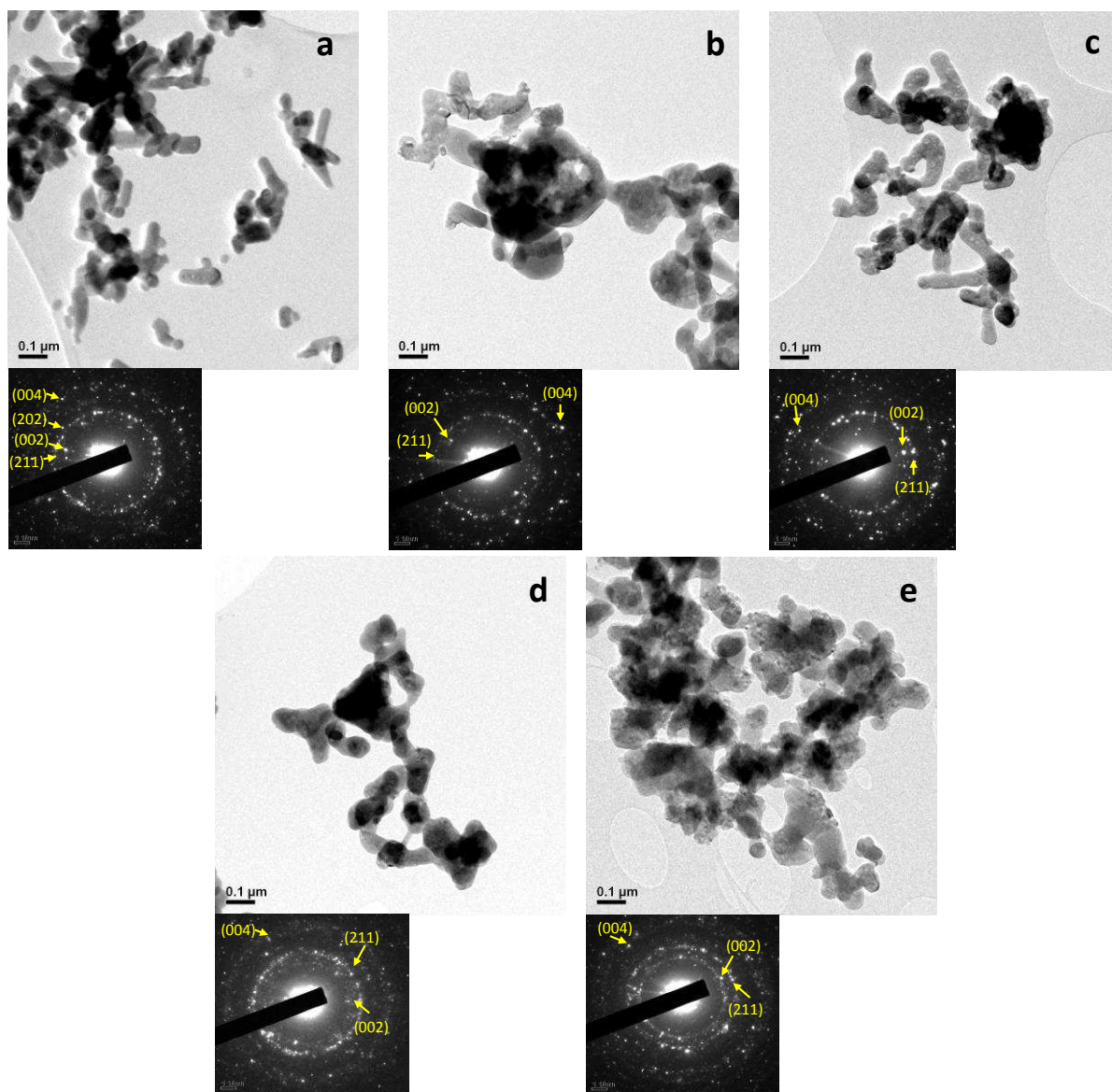


Figure 4. TEM pictures and SAED patterns collected on samples HAp (a) TiHA8 (b) TiHA17 (c) TiHA25 (d) and TiHA50 (e).

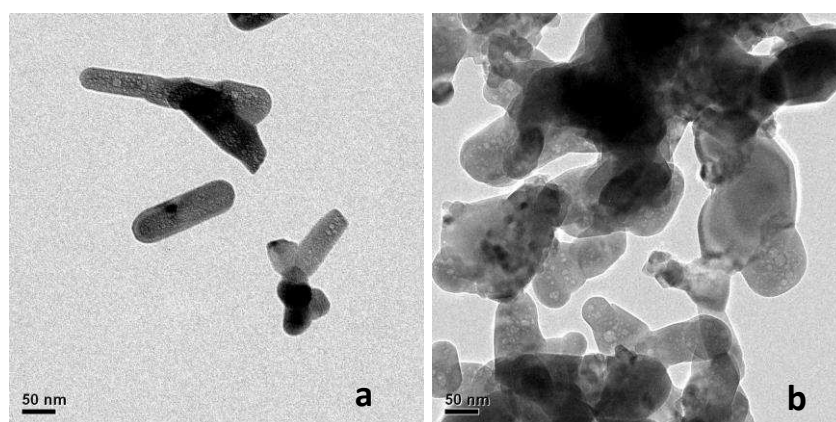


Figure 5. TEM pictures of HAp (a) and TiHA (b) at high magnification showing NPs nanopores.

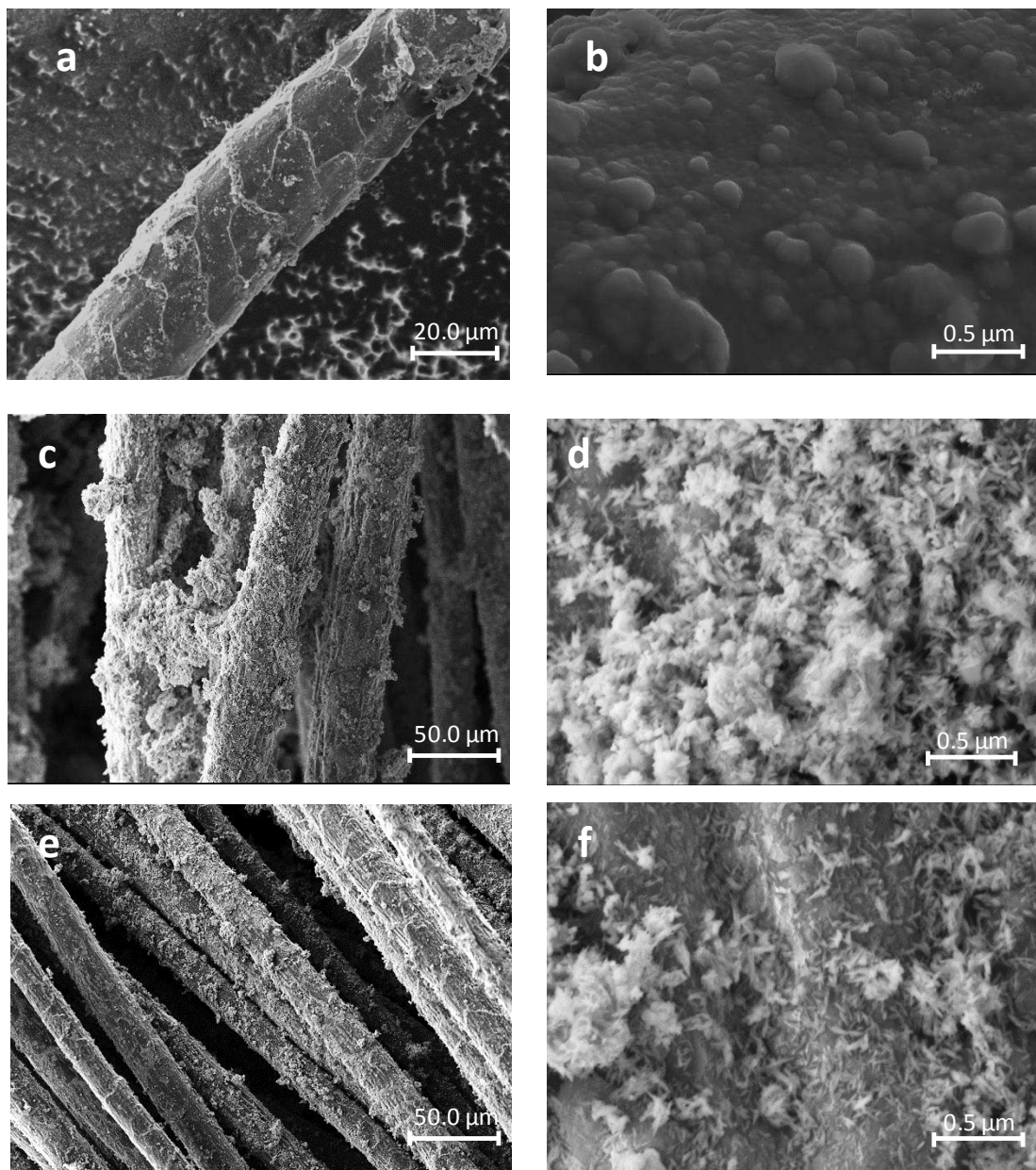


Figure 6. SEM pictures of wool fibers coated by PPy mineralized with TiHA25. Surface of the WAP fibers after mineralization at increasing magnification (a,b); **Surface of the WEAP5(c,d) and WEAP10 (e,f) fibers** after mineralization at increasing magnification

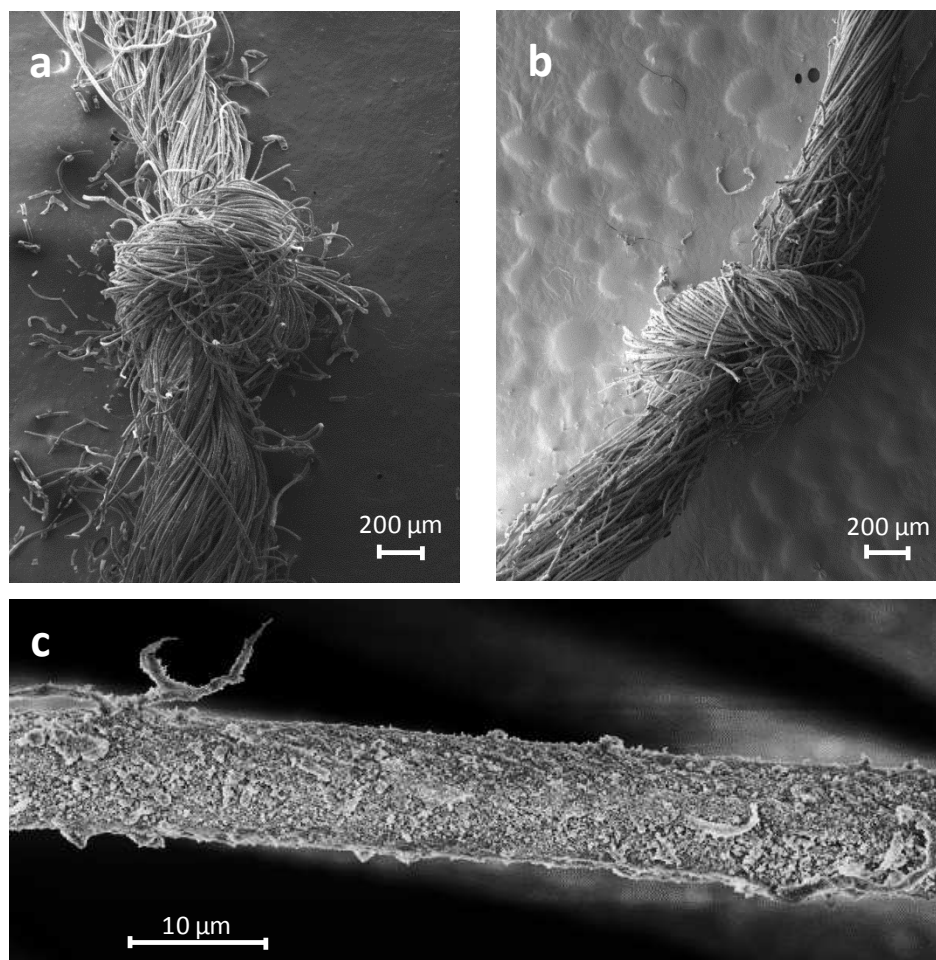


Figure 7. SEM pictures of knotted WEAP5 yarns before (a) and after (b) bio-inspired mineralization, with a micrograph of mineralized WEAP5 after dipping at 40°C in ethanol for 15 minutes (c).

Table 1. Cell parameters calculated by Rietveld analysis of the XRD spectra reported in Fig.1. Crystallinity degree was calculated applying the formula described in eqn(1)^a. Standard deviation is < 1%.

	HA	TiHA8	TiHA17	TiHA25	TiHA50
a (Å)	9,424	9.425	9.427	9.427	9.441
c (Å)	6,884	6.889	6.894	6.892	6.889

V(Å³)	529,5	529.9	530.5	530.4	531.7
Cristallinity (%)^a	67	64	55	54	52
IR-SF	2.06	1.24	2.02	1.52	1.63

Table 2. Phase composition determined by Rietveld refinement of the XRD spectra collected on samples treated at 700°C for 6 hours. Standard deviation is < 1%

	HAp	TiHA8	TiHA17	TiHA25	TiHA50
HA (%)	100	94,5	74,2	75,7	67,4
b-TCP (%)	0	5,5	23,3	15,3	17,5
TiO₂ (an) (%)	0	0	2,5	9,0	15,1

Table 3. Chemical composition of synthesized HAs determined by ICP-OES, together with carbonation determined by TGA and specific surface area determined by BET. Values are an average of 3 analysis. Error is reported as standard deviation

	HA	TiHA8	TiHA17	Ti-HA25	TiHA50
Ca wt.%	36.74 ± 0.14	37.91 ± 0.56	36.97 ± 0.33	32.21 ± 0.26	28.08 ± 0.40
P wt.%	15.09 ± 0.07	16.64 ± 0.08	14.59 ± 0.10	14.05 ± 0.06	12.24 ± 0.06
Ti wt.%	-	2.08 ± 0.01	4.48 ± 0.04	6.32 ± 0.03	10.01 ± 0.1
^aCO₂ wt.%^a	1.46 ± 0.07	1.61 ± 0.08	1.80 ± 0.09	1.72 ± 0.12	1.57 ± 0.08
Ca/P molar	1.69 ± 0.03	1.76 ± 0.03	1.96 ± 0.07	1.77 ± 0.04	1.77 ± 0.05
(Ti+Ca)/P molar	-	1.84 ± 0.03	2.16 ± 0.06	2.06 ± 0.03	2.30 ± 0.04
Ca/(P+Ti) molar	-	1.65±0.05	1.64±0.05	1.38±0.06	1.16±0.05
Ti/P molar	-	7.66±0.40	16.95±0.85	27.42±0.91	49.83±1.00

^b SSA m ² /g	84±9	101 ± 10	123 ± 12	146 ± 13	134 ± 13
------------------------------------	------	----------	----------	----------	----------

^a Determined by TGA

^b Determined by BET